

## Hierarchical $\text{TiO}_2@\text{Ru}_{0.9}\text{Ir}_{0.1}\text{O}_2$ as Highly-durable Electro-catalyst for Oxygen Evolution Reaction

Wankai Zhou<sup>1,2</sup>, Li Ma<sup>2</sup>, Tigang Duan<sup>2,\*</sup>, Yonglei Xin<sup>2,\*</sup>, Xianze Gao<sup>2,3</sup>, Likun Xu<sup>2</sup>

<sup>1</sup> School of Materials Science and Engineering, Wuhan University of Technology, Wuhan 430070, China;

<sup>2</sup> State Key Laboratory for Marine Corrosion and Protection, Luoyang Ship Material Research Institute (LSMRI), Qingdao 266237, China;

<sup>3</sup> Key Laboratory of Superlight Materials and Surface Technology of Ministry of Education, College of Material Science and Chemical Engineering, Harbin Engineering University, Harbin 15001, Heilongjiang, China

\*E-mail: [duantigang@sunrui.net](mailto:duantigang@sunrui.net), [xinyi@sunrui.net](mailto:xinyi@sunrui.net)

Received: 15 April 2022 / Accepted: 29 May 2022 / Published: 4 July 2022

Hierarchical acid-durable  $\text{TiO}_2@\text{Ru}_{0.9}\text{Ir}_{0.1}\text{O}_2$  electrodes were designed and fabricated through the combination of in-situ hydrothermal method and thermal pyrolysis. The evolution of intermediate layers for electrodes were realized from nanosheets and nanosheet-nanowire hybrids to nanowires through regulating the hydrothermal time. Then morphology effects of  $\text{TiO}_2$  nanostructures were investigated. Results show that the crystal planes of (101) and (110) of rutile-phase  $\text{RuO}_2$  are exposed. The oxygen evolution potential of  $\text{TiO}_2$ -nanowire@ $\text{Ru}_{0.9}\text{Ir}_{0.1}\text{O}_2$  is about 51 mV lower than that of Ti-matrix electrode with a current density of  $30 \text{ A g}^{-1}$ . Chronoamperometric results tested at 1.541 V vs RHE that the response current of  $\text{TiO}_2$ -nanowire@ $\text{Ru}_{0.9}\text{Ir}_{0.1}\text{O}_2$  is 10.9 times as much as that of Ti-matrix electrode ( $4.46$  vs  $0.41 \text{ A g}^{-1}$ ), while the electrochemically active surface area of  $\text{TiO}_2$ -nanowire matrix electrode is much higher than that of Ti-matrix one ( $9.115$  vs  $1.896 \text{ mF}$ ). Cyclic durability results of electrodes tested in the acid solution show that the. Thus the introduction of  $\text{TiO}_2$  nanostructures benefits to enhance the long-term durability of electrode materials.

**Keywords:**  $\text{RuO}_2/\text{IrO}_2$  mixed oxide; OER in acidic media; high acid-cycling durability; morphology evolution.

### 1. INTRODUCTION

Hydrogen, as one of the most promising renewable energy fuels, has been extensively explored to replace fossil fuels and reduce greenhouse gas emissions [1-2]. Electrochemical Water splitting into hydrogen, which involves the evolution of molecular hydrogen (cathode) and oxygen (anode), has been considered as one of the most probable commercialization practices [3-6]. However, due to the limitation

of the sluggish four-electron dynamics and the high oxidative potential, the electrochemical oxygen evolution process is currently not economically available in comparison with the fast hydrogen evolution process involving a two-electron transfer [7-9].

Recently, an increasing number of promising electrocatalyst materials, such as noble metals, metal oxides/hydroxides, carbon nanomaterials, metal phosphide/phosphate catalysts, metal nitride/boride/sulfide catalysts, and so on, have been proven to perform good catalytic activities toward oxygen evolution reaction (OER) [10-15]. Thereinto, metal oxide families including perovskite-type oxides, spinel-type oxides and layered double hydroxides have been revealed to exhibit remarkable activities [16-19]. In contrast to that case in alkaline electrolytes, electrochemical water splitting in the acidic solution has been generally accepted as energy conversion devices with a huge barrier avoiding the detrimental accumulation of carbonates as contaminants, which frequently occurs in the alkaline environment and reduces the lifetime of electrochemical devices [20].

However, the harsh oxidation environment for water splitting in the acidic medium makes a limitation to perform a long-term stability for most of OER electrocatalysts [21]. For decades, to overcome the limitation of electrochemical water splitting in the acidic environment, a huge quantity of research work has been conducted to explore perdurable and high-efficiency OER electrocatalysts [22-25]. In particular, noble metal-based materials and their derivatives such as RuO<sub>2</sub> and IrO<sub>2</sub> have been reported to perform excellent electrocatalytic activities for OER [24]. Ruthenium element, as one of cheapest platinum group metals, has been greatly concerned as an ideal alternative material, because of the relatively low cost and abundant reserves with reference to iridium [26].

Typically, Ru-based oxides have been proven unstable under high anodic current density, and this leads to the deterioration of RuO<sub>2</sub>-based electrocatalysts, which can be relevant to various pernicious microstructure evolutions of high oxidation state catalytic active phases such as oxidative dissolution, structural reconstruction, metal precipitation and erratic aggregation [27]. It's worth noting that the exfoliation of catalytic active species from current collector such as Ti substrate in a dimensionally stable anode (DSA) during OER process is also another crucial adjective stability problem [28]. Therefore, it is highly desirable to design RuO<sub>2</sub>-based catalysts to further optimize acidic OER catalytic lifetime to reduce the decrease of high catalytic activity of the electrode materials.

In this paper, various hydrothermal in-situ TiO<sub>2</sub> nanostructures were introduced between the substrate and the catalyst coating in order to improve the long-term stability and the catalytic activity of electrode applied in the acidic medium. Morphology, crystalline form and coating structure and so on were characterized through field-emission scanning electron microscope, X-ray diffractometer, transmission electron microscope, X-ray photoelectron spectroscopy and so on. Electrochemical behaviors were studied through linear sweeping voltammetry, electrochemical impedance spectroscopy, cyclic voltammetry and so on. Experimental results showed that the introduction of hydrothermal TiO<sub>2</sub> nanostructures enhances the activity and the stability of electrodes in the acid medium.

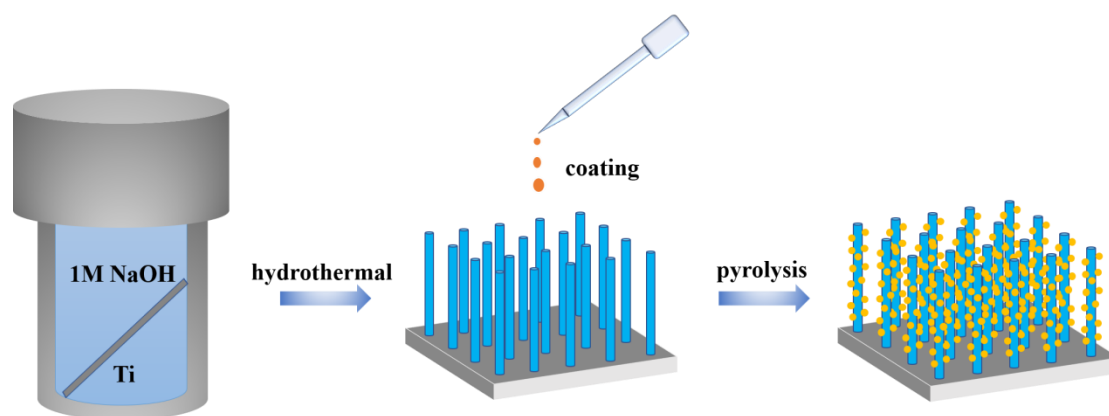
## 2. EXPERIMENTAL

### 2.1 Electrode preparation

Before the formation of TiO<sub>2</sub> nanostructures, Ti foils (5×1.5×0.1 cm<sup>3</sup>, TA2) were ultrasonically

cleaned through ultrapure water, ethyl alcohol and acetone, respectively, and then went through a surface treatment in 10wt% oxalic acid solution with 80°C for 4h. The treated Ti foils were washed using ultrapure water and acetone, and then were immersed in absolute ethanol for use. Then, the dried Ti foil was placed against the wall of Teflon-lined stainless steel autoclave filled with 50 mL of 1 mol L<sup>-1</sup> NaOH solution. The hydrothermal etching reactions were conducted in a preheated oven at 180 °C for 12 h, 200 °C for 12 h and 24 h, respectively. After the hydrothermal processing, samples were washed with ultrapure water for several times, and were immersed into 0.5 mol L<sup>-1</sup> hydrochloric acid for 12 h for the completely ion exchange between Na<sup>+</sup> and H<sup>+</sup>. Finally, samples were calcinated at 500 °C for 2 h to convert the amorphous TiO<sub>2</sub> to the crystallized TiO<sub>2</sub>. Hierarchical TiO<sub>2</sub> structures with morphologies of sheets, sheet-nanowire hybrid, and nanowires were obtained, and were marked as TNS, TNSW and TNW, respectively.

The coating precursor solution was prepared through 10 mol% H<sub>2</sub>IrCl<sub>6</sub>·6H<sub>2</sub>O and 90 mol% RuCl<sub>3</sub>·xH<sub>2</sub>O were mixed, dissolved and stirred in n-butyl alcohol for 30 min, obtaining 0.3 mol L<sup>-1</sup> precursor solution. Catalyst coatings were prepared by the drop-casting method. After precursor solution was drop-cast, samples were firstly dried for 20 min at 130 °C to evaporate the solvent, and then annealed in 500 °C air atmosphere for 20 min. This process was successively repeated up to five times, and the last calcination was performed for 1h to ensure the sufficient oxidation. Electrode samples based on Ti plate, TiO<sub>2</sub> nanosheets, TiO<sub>2</sub> nanosheet-nanowire hybrids and TiO<sub>2</sub> nanowires were marked as Ti/Ru<sub>0.9</sub>Ir<sub>0.1</sub>O<sub>2</sub>, TNS@Ru<sub>0.9</sub>Ir<sub>0.1</sub>O<sub>2</sub>, TNSW@Ru<sub>0.9</sub>Ir<sub>0.1</sub>O<sub>2</sub>, and TNW@Ru<sub>0.9</sub>Ir<sub>0.1</sub>O<sub>2</sub>, respectively. Electrode samples were weighed, and the average specific weight loadings of RuO<sub>2</sub>-IrO<sub>2</sub> catalysts are 0.327, 0.302, 0.323 and 0.320 mg cm<sup>-2</sup>. The preparation process of TNW/Ru<sub>0.9</sub>Ir<sub>0.1</sub>O<sub>2</sub> electrode was shown in Scheme 1.



**Scheme 1.** Illustration of the synthesis of the TNW@Ru<sub>0.9</sub>Ir<sub>0.1</sub>O<sub>2</sub> electrode.

## 2.2 Electrode characterizations

X-ray diffraction (XRD) patterns were recorded on an X-ray diffractometer (Bruker D8 Advance, Germany) at a scan rate of 5° min<sup>-1</sup> in the range from 20° to 90°. The morphologies of samples were characterized using a field-emission scanning electron microscope (FESEM, ULTRA55, Germany) and a transmission electron microscope (TEM, JEM 2100F, Japan) operating at 200 kV.

### 2.3 Electrochemical experiments

All the electrochemical measurements were performed using a traditional three-electrode electrochemical cell at the room temperature. A saturated calomel electrode (SCE) and a Pt wire were used as reference and counter electrodes, respectively. 0.5 mol L<sup>-1</sup> H<sub>2</sub>SO<sub>4</sub> solution was used as the electrolyte solution. Electrode samples with exposed areas of 1 cm<sup>2</sup> were used as working electrodes. All the measurements were performed using a Biologic VMP3 electrochemical workstation equipped with EC-Lab Software. Cyclic voltammetry (CV) was performed from 0.6 V vs SCE to 0.7 V vs SCE with scanning rates of 5, 10, 25, 50, 100, 200, 400, and 800 mV s<sup>-1</sup>. Then the plots of the current versus the scanning rate Tafel curves were obtained from liner sweeping voltammetric curves (LSV) with a scan rate of 1 mV s<sup>-1</sup>. The chronoamperometric experiments were carried out at 1.3 V (vs. SCE). In all the electrochemical figures, the SCE potentials were converted to RHE potentials according to the following equation:

$$E_{RHE} = E + E_{SCE}^{\ominus} + 0.059 pH \quad (1)$$

### 3. RESULTS AND DISCUSSION

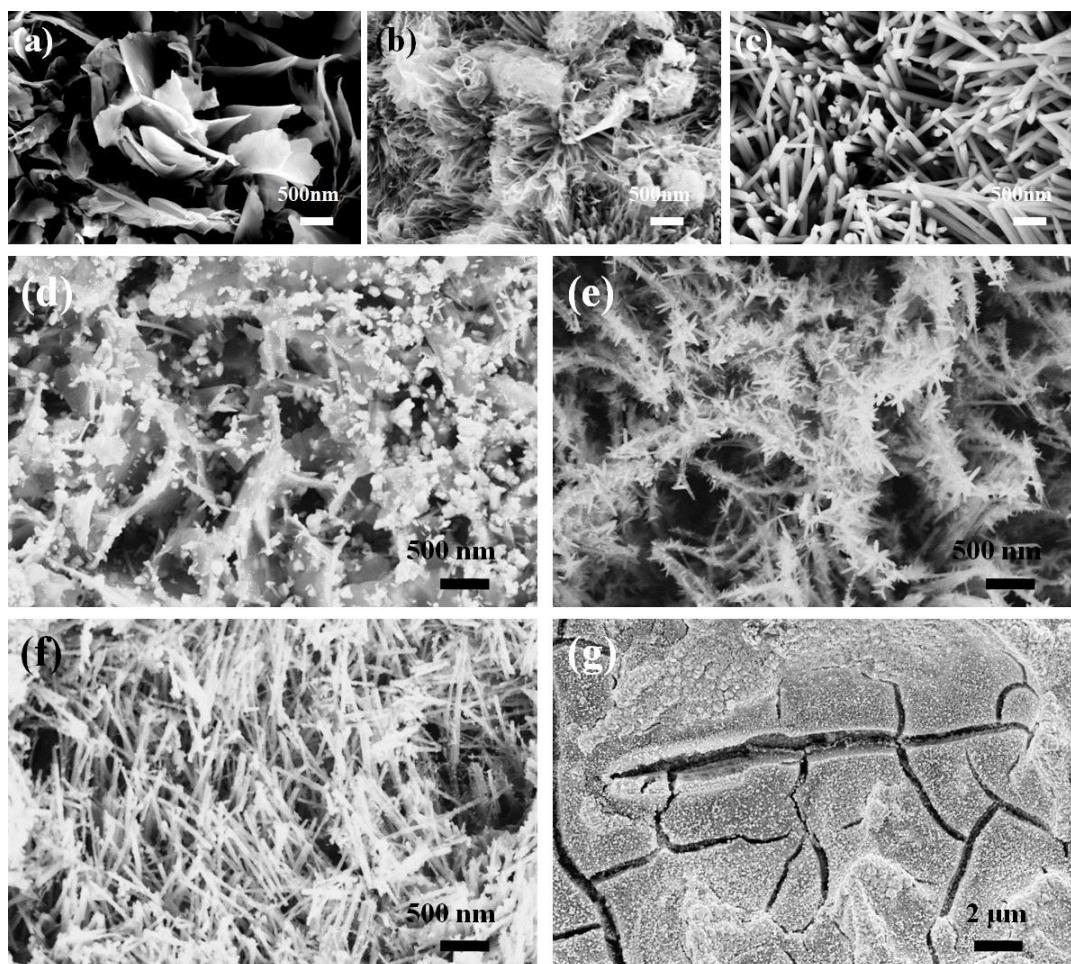


**Figure 1.** FESEM images of TiO<sub>2</sub> nanostructures and the hierarchical TiO<sub>2</sub>/Ru<sub>0.9</sub>Ir<sub>0.1</sub>O<sub>2</sub> electrodes: (a) TiO<sub>2</sub> nanosheets, (b) TiO<sub>2</sub> nanosheet-wire hybrids, (c) TiO<sub>2</sub> nanowires, (d) TNS@Ru<sub>0.9</sub>Ir<sub>0.1</sub>O<sub>2</sub>, (e) TNSW@Ru<sub>0.9</sub>Ir<sub>0.1</sub>O<sub>2</sub>, (f) TNW@Ru<sub>0.9</sub>Ir<sub>0.1</sub>O<sub>2</sub>, and (g) complanate Ti/Ru<sub>0.9</sub>Ir<sub>0.1</sub>O<sub>2</sub> electrodes.

As shown in Figure 1, three kinds of TiO<sub>2</sub> nanostructures (nanosheets, nanosheet-wire hybrids and nanowires, respectively) were obtained through the in-situ hydrothermal etching method under different hydrothermal treatments and they are inclined to randomly distribute on the Ti substrate. After the hydrothermal reaction for 12 h at a low reaction temperature of 180 °C, some short and curly nanosheet aggregates are formed on the surface of Ti substrate as shown in Figure 1a, and the nanosheet thickness is about 20 nm. As shown in Figure 1b, when the hydrothermal reaction temperature increases to 200 °C, TiO<sub>2</sub> nanosheets elongate in the length wise direction and shrank in the cross direction, forming the narrow and gracile nanowires at the end of nanosheets with a small remaining portion of the original nanosheet morphology. When the reaction time further increases with a fixed reaction temperature of 200 °C, the nanosheet-wire hybrid structure completely transforms into hierarchical nanowires with a diameter of 100-200 nm.

FESEM images of TiO<sub>2</sub>@Ru<sub>0.9</sub>Ir<sub>0.1</sub>O<sub>2</sub> electrodes prepared by the thermal pyrolysis method are shown in Figures 1 (d-f). For the sample prepared by a hydrothermal treatment at 180 °C for 12 h, the edges of TiO<sub>2</sub> nanosheets are uniformly covered with RuO<sub>2</sub>-IrO<sub>2</sub> mixed nanocrystals (shown in Figure 1d). As the hydrothermal temperature increases to 200°C, a mass of dendritic-like RuO<sub>2</sub>-IrO<sub>2</sub> nanocrystals transformed from nanoparticles are distributed uniformly on the surface of curved nanosheet-wire hybrids, which may be ascribed to the driving force caused by the diffusion of amorphous Ru(OH)<sub>3</sub> nanoparticles on the surface of flexuous TiO<sub>2</sub> nanowires, and the internal stress associated with the phase formation on the interface [29]. As shown in Figure 1f, the original structure of nanowires is kept after the coating of conductive RuO<sub>2</sub>-IrO<sub>2</sub> nanoparticles on the nanowires. It can be supposed that abundant active sites for the nucleation of active materials exist on the erect and thick TiO<sub>2</sub> nanowire and can provide a large active specific surface area for refining the crystal grains and suppressing the growth of the crystal grains thermodynamically. For comparison, complanate Ti/Ru<sub>0.9</sub>Ir<sub>0.1</sub>O<sub>2</sub> electrode mainly consists of bulk active materials and many irregular muddy cracks that are not conducive to maintaining the electrode stability in service.

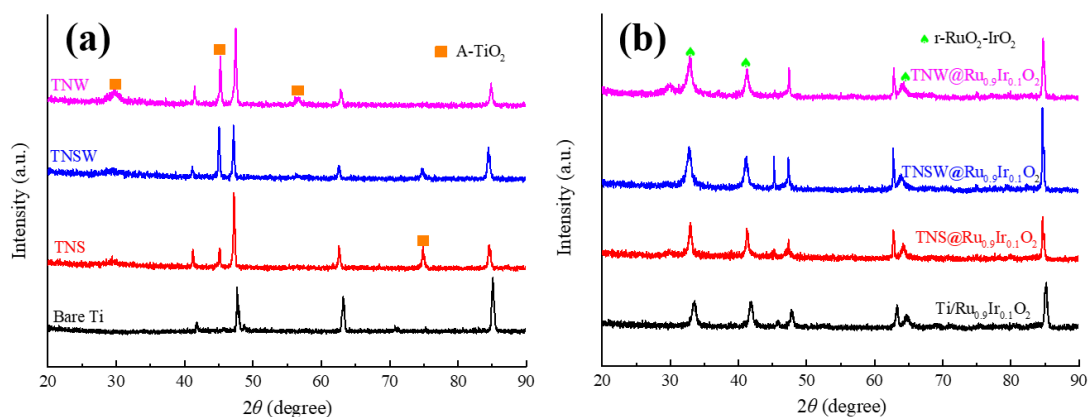


**Figure 2.** XRD patterns of (a) bare Ti and TiO<sub>2</sub> nanostructures synthesized through the hydrothermal treatment; (b) Ru<sub>0.9</sub>Ir<sub>0.1</sub>O<sub>2</sub> electrodes with various TiO<sub>2</sub> structures.

XRD patterns of TiO<sub>2</sub> nanostructures are shown in Figure 2a, and results agree well with the

crystal structure of the anatase  $\text{TiO}_2$  phase (PDF#21-1272) and no other phase is observed except peaks of Ti matrix (PDF#44-1294), indicating that the obtained  $\text{TiO}_2$  is well crystallized after calcinated at  $500\text{ }^\circ\text{C}$  for 1 h. With the extension of hydrothermal time, the diffraction peak intensity increases, indicating the amount of crystallized  $\text{TiO}_2$  increases. XRD patterns of Ru-Ir mixed oxide electrodes shown in Figure 2b display a certain degree of right shift referring to the standard card of rutile phase  $\text{RuO}_2$  (PDF#43-1027) and  $\text{IrO}_2$  (PDF#43-1019). Thereinto, the diffraction peaks of control sample displays a largest right shift. It is well known that rutile phase  $\text{RuO}_2$  and  $\text{IrO}_2$  have the extremely similar crystal structure and that the ionic radii of  $\text{Ru}^{4+}$  and  $\text{Ir}^{4+}$  are nearly the same, which are favorable to the formation of solid solution [27]. Due to the formation of solid solution, the crystal plane spacing gets closer, leading to the grain refinement. It is found that the half-height width for the diffraction peaks of electrodes becomes larger after the introduction of  $\text{TiO}_2$ , indicating the  $c$  size is much smaller than the control group. Moreover,  $\text{TNW@Ru}_{0.9}\text{Ir}_{0.1}\text{O}_2$  electrode has the largest half-height width, indicating the smallest crystal size of the prepared electrode according to the Scherrer Formula [28]. It can be assumed that  $\text{TiO}_2$  nanowires provide a large number of nucleation sites for the adhesion of  $\text{RuO}_2/\text{IrO}_2$  mixed nanocrystalline, inhibiting the formation of Ru/Ir solid solution but refining the grains.

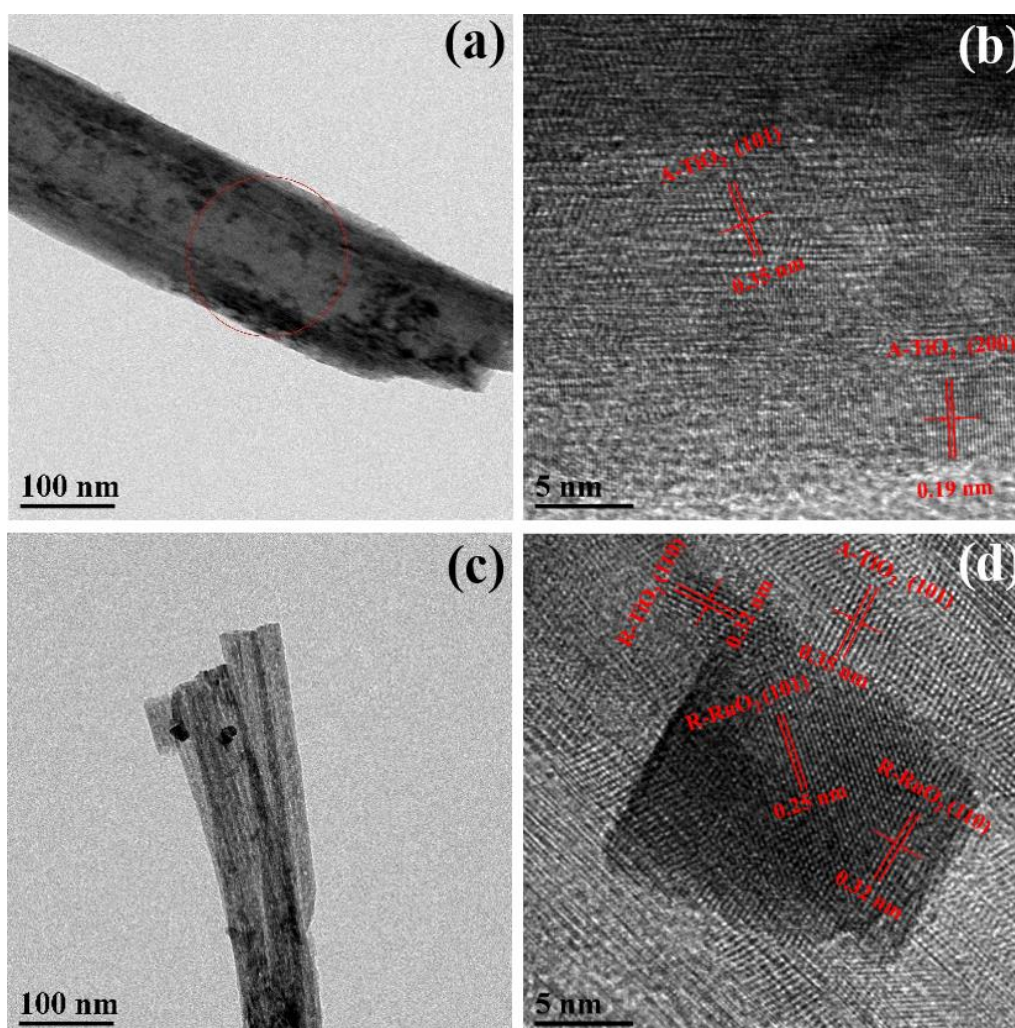


**Figure 3.** TEM images of (a) single  $\text{TiO}_2$  nanowire (c)  $\text{TNW@Ru}_{0.9}\text{Ir}_{0.1}\text{O}_2$  electrode; HRTEM images of (b) single  $\text{TiO}_2$  nanowire (d)  $\text{TNW@Ru}_{0.9}\text{Ir}_{0.1}\text{O}_2$  electrode.

Typical transmission electron microscopy images are shown in Figure 3. The synthesized TiO<sub>2</sub> nanowire has a diameter of 100 nm and a length of 600 nm, and presents straight sides and irregular ends. And RuO<sub>2</sub>/IrO<sub>2</sub> mixed nanocrystals with the grain sizes of 10-20 nm grow on the surface of TiO<sub>2</sub> nanowires. The detailed crystal structures of TiO<sub>2</sub> nanowire and TNW@Ru<sub>0.9</sub>Ir<sub>0.1</sub>O<sub>2</sub> were carefully characterized by high-resolution TEM as shown in Figures 3b and 3d. Characteristic interplanar spacings of TiO<sub>2</sub> nanowire sample are 0.35 and 0.19 nm, corresponding to the lattice planes of (101) and (200), respectively, consistent with the results of XRD. The lattice fringe of TNW@Ru<sub>0.9</sub>Ir<sub>0.1</sub>O<sub>2</sub> sample shows the expected interplanar spacings of 0.32 and 0.25 nm corresponding to the lattice planes of (110) and (101), respectively. It is indicated that the dominant crystal plane of mixed RuIr oxides is the plane of (110), agreeing well with the plane of (110) of rutile TiO<sub>2</sub>. This result can be favorable to the growth of metal oxides with good binding forces, and improves the electrode stability as well as promoting the catalytic activity.

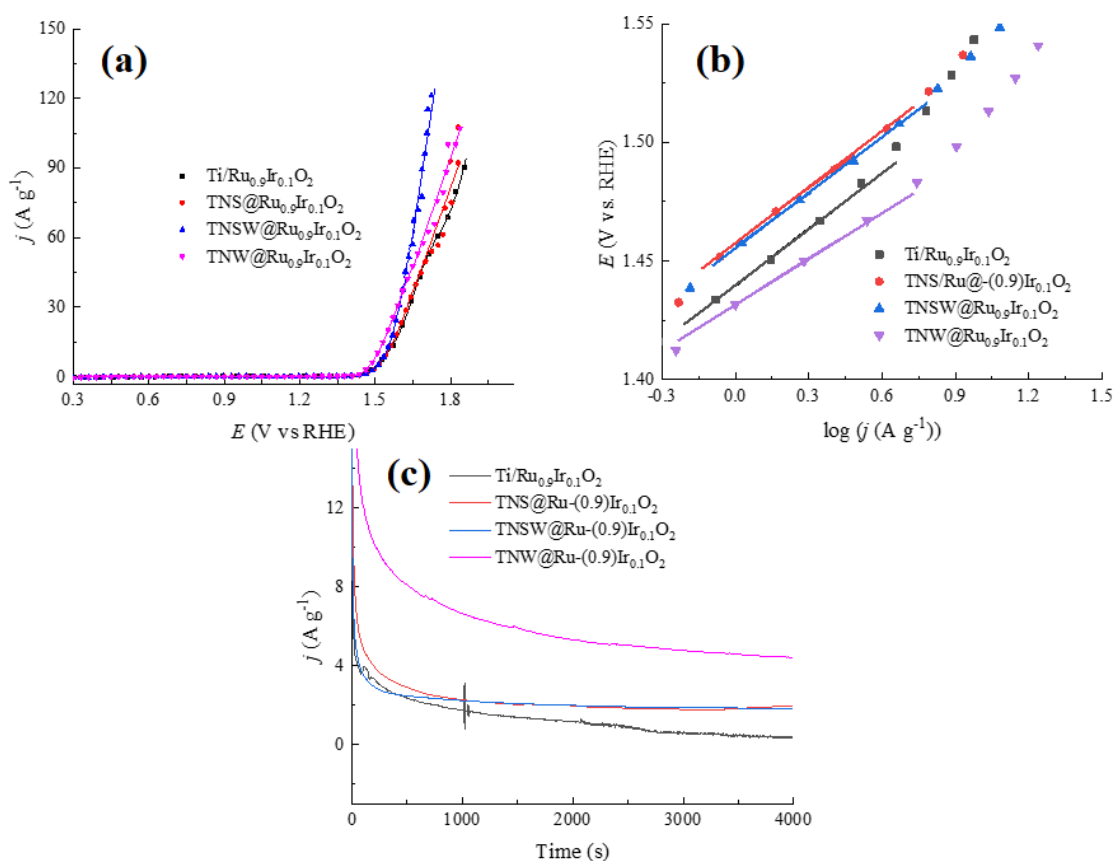


**Figure 4.** (a) LSV curves, (b) Tafel plots and (c) chronoamperometric plots of electrode samples. Scanning rates in (a) and (b) are 1 mV s<sup>-1</sup>. The given potential in (c) is 1.541 V vs RHE.

Electrocatalytic OER activities of Ru<sub>0.9</sub>Ir<sub>0.1</sub>O<sub>2</sub> electrodes with different morphologies were measured in 0.5 mol L<sup>-1</sup> H<sub>2</sub>SO<sub>4</sub> solution, and results are shown in Figure 4. Tafel slopes were fitted by the linear part taken from the LSV curves. Kinetic parameters and the oxygen evolution potential were obtained from LSV curves and are presented in Table 1. Due to the intrinsic outstanding activities of

electrocatalysts containing RuO<sub>2</sub>, TNW@Ru<sub>0.9</sub>Ir<sub>0.1</sub>O<sub>2</sub> shows the optimal OER performance, proven by the LSV curves (Figure 4a), which only needs 1.587 V vs RHE to reach the current density of 30 A g<sup>-1</sup>, much lower than that of control samples (1.638 V vs RHE), TNS@Ru<sub>0.9</sub>Ir<sub>0.1</sub>O<sub>2</sub> (1.627 V vs RHE) and TNSW@Ru<sub>0.9</sub>Ir<sub>0.1</sub>O<sub>2</sub> (1.596 V vs RHE), respectively.

Figure 4b shows the fitting results of linear polarization regions in Tafel plots. Observing from Figure 4b, it is obvious that TNW@Ru<sub>0.9</sub>Ir<sub>0.1</sub>O<sub>2</sub> electrode has rapider electrochemical reaction rate inferred from the larger exchange current density ( $j_0=3.24 \text{ A}\cdot\text{g}^{-1}$ ) compared to the control sample ( $j_0=3.16 \text{ A}\cdot\text{g}^{-1}$ ). The Tafel slope decreases as the transitions from TNS@Ru<sub>0.9</sub>Ir<sub>0.1</sub>O<sub>2</sub> (75.21 mV dec<sup>-1</sup>) to TNW@Ru<sub>0.9</sub>Ir<sub>0.1</sub>O<sub>2</sub> (64.37 mV dec<sup>-1</sup>), suggesting the enhanced OER capacity owing to the morphology transition of hydrothermal TiO<sub>2</sub> nanostructures. Additionally, the chronoamperometric experiments were also carried out at 1.541 V (vs. RHE), and the stable response current densities are about 0.41, 1.79, 1.91 and 4.46 A g<sup>-1</sup> for Ti/ Ru<sub>0.9</sub>Ir<sub>0.1</sub>O<sub>2</sub>, TNS@Ru<sub>0.9</sub>Ir<sub>0.1</sub>O<sub>2</sub>, TNSW@ Ru<sub>0.9</sub>Ir<sub>0.1</sub>O<sub>2</sub> and TNW@ Ru<sub>0.9</sub>Ir<sub>0.1</sub>O<sub>2</sub>, respectively, showing TNW@ Ru<sub>0.9</sub>Ir<sub>0.1</sub>O<sub>2</sub> possesses the highest electrochemical activity. Table 2 lists a comparison of OER performance with some representative electrocatalysts, and shows that TNW@Ru<sub>0.9</sub>Ir<sub>0.1</sub>O<sub>2</sub> in this work has a lower Tafel slope.

**Table 1.** kinetic parameters and response curenets obtained from Figure 4.

Sample	$b_a(\text{mV dec}^{-1})$	$j_0(\text{A}\cdot\text{g}^{-1})$	$j(\text{A}\cdot\text{g}^{-1} \text{ at } 1.541 \text{ V})$
Ti/Ru <sub>0.9</sub> Ir <sub>0.1</sub> O <sub>2</sub>	78.93	3.16	0.41
TNS@Ru <sub>0.9</sub> Ir <sub>0.1</sub> O <sub>2</sub>	75.21	3.11	1.79
TNSW@Ru <sub>0.9</sub> Ir <sub>0.1</sub> O <sub>2</sub>	75.21	3.20	1.91
TNW@Ru <sub>0.9</sub> Ir <sub>0.1</sub> O <sub>2</sub>	64.37	3.24	4.46

**Table 2.** comparison of OER performance with some representative electrocatalysts.

Sample	Loading amount(mg cm <sup>-2</sup> )	electrolyte	$b_a(\text{mV dec}^{-1})$	Ref.
Ti/Ru <sub>0.9</sub> Ir <sub>0.1</sub> O <sub>2</sub>	0.327	0.5 mol L <sup>-1</sup> H <sub>2</sub> SO <sub>4</sub>	78.93	This work
TNW@Ru <sub>0.9</sub> Ir <sub>0.1</sub> O <sub>2</sub>	0.320	0.5 mol L <sup>-1</sup> H <sub>2</sub> SO <sub>4</sub>	64.37	This work
Ti/IrO <sub>2</sub> -RuO <sub>2</sub> @Ru	N/A	0.5 mol L <sup>-1</sup> H <sub>2</sub> SO <sub>4</sub>	~55	[30]
Ru@IrOx	0.275	0.05 mol L <sup>-1</sup> H <sub>2</sub> SO <sub>4</sub>	69.1	[31]

To analyze the electrochemical activities of electrodes, the electrochemically active surface area for each electrode was estimated from the electrochemical double-layer capacitance of the catalytic surface based on the cyclic voltammetry [32-34]. To avoid the pseudocapacitance region, the potential range of 0.6~0.7 V (vs SCE) was tested with various sweeping rates of 0.005, 0.01, 0.025, 0.05, 0.1, 0.2, 0.4, and 0.8 V s<sup>-1</sup>. The relationship between the current ( $I$ ) and the sweeping rate ( $\nu$ ) was plotted, and results were shown in Figure 5. The electrochemical double-layer capacitance ( $C_{DL}$ ) was calculated according to the equation [34]:

$$C_{DL} = I/\nu \tag{2}$$

The plot of  $I$  as a function of  $\nu$  displays a straight line, thus  $C_{DL}$  value obtained from the slope. Calculated results show that the values of electrodes are 1.896, 5.315, 5.129 and 9.115 mF, respectively, suggesting the greatest electrochemical activity for TNW@ Ru<sub>0.9</sub>Ir<sub>0.1</sub>O<sub>2</sub>.

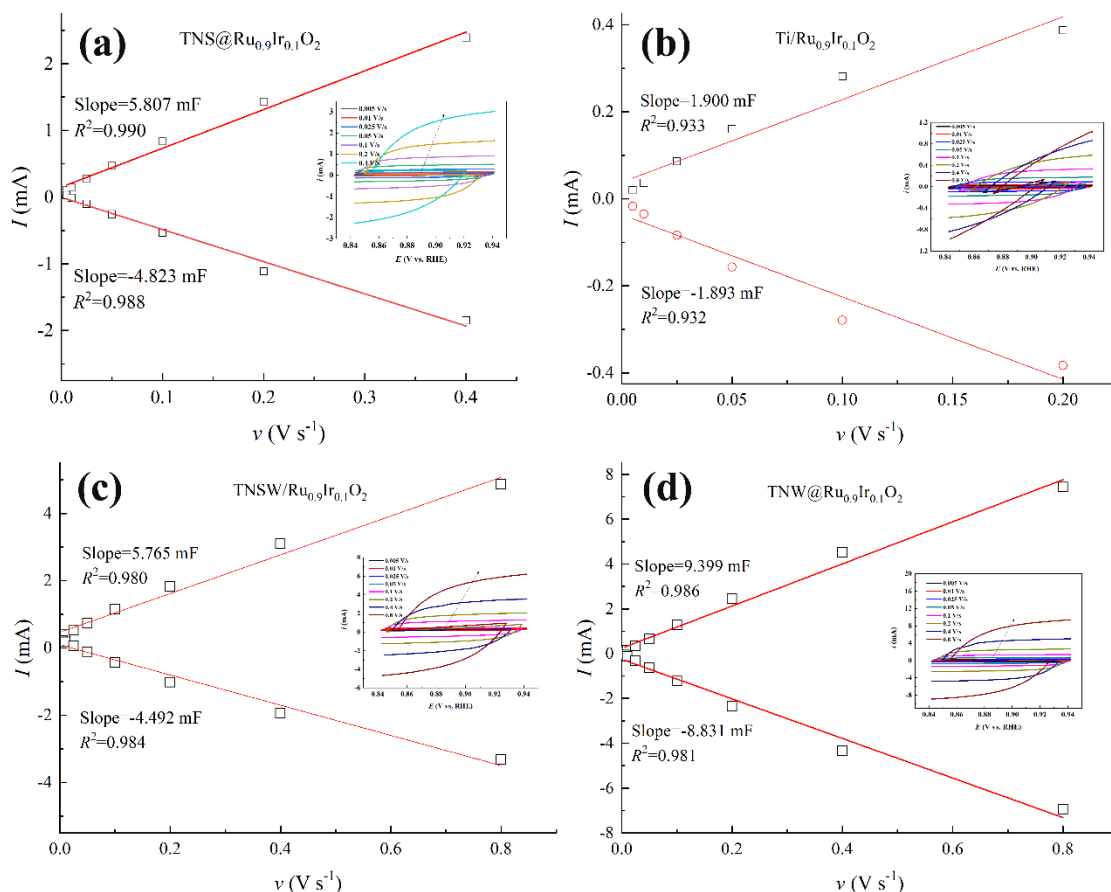


**Figure 5.** Double-layer capacitance measurements for determining electrochemically active surface areas of various electrodes: (a)Ti/Ru<sub>0.9</sub>Ir<sub>0.1</sub>O<sub>2</sub>, (b) TNS@ Ru<sub>0.9</sub>Ir<sub>0.1</sub>O<sub>2</sub>, (c) TNSW@ Ru<sub>0.9</sub>Ir<sub>0.1</sub>O<sub>2</sub>, (d) TNW@ Ru<sub>0.9</sub>Ir<sub>0.1</sub>O<sub>2</sub>. Insets are cyclic voltammograms measured in a non-Faradaic region of the voltammogram with sweeping rates of 0.005, 0.01, 0.025, 0.05, 0.1, 0.2, 0.4 and 0.8 V s<sup>-1</sup>.

The significantly increased electrochemical double-layer capacitance can be attributed to high specific surface area of TiO<sub>2</sub> nanowire interlayers which provide a large number of catalytically active sites caused by the grain size refinement. It is likely that the high specific surface area of TiO<sub>2</sub> nanowires and the uniform distribution of grain-refined RuO<sub>2</sub>-IrO<sub>2</sub> mixed nanocrystals provide a large number of catalytically active sites, which makes the indispensable effect of morphology engineering prominent on electrode materials design.

In this paper, the cycling stability of electrode was tested through cyclic voltammetry with a scan rate of 20 mV s<sup>-1</sup> for 1st and 1000th cycles and 100 mV s<sup>-1</sup> for other cycles. Besides, LSV curves were performed to compare the increase of potential at the current density of 30 A g<sup>-1</sup> as well. The OER

potential of TNW@Ru<sub>0.9</sub>Ir<sub>0.1</sub>O<sub>2</sub> increases marginally from 1.643 V vs RHE to 1.644 V vs RHE at 30 A g<sup>-1</sup> from 1st to 1000th cycle while that of control sample arises from 1.693 V vs RHE to 1.724 V vs RHE, suggesting that TNW@Ru<sub>0.9</sub>Ir<sub>0.1</sub>O<sub>2</sub> has higher stability after cycling than Ti/Ru<sub>0.9</sub>Ir<sub>0.1</sub>O<sub>2</sub> electrode.

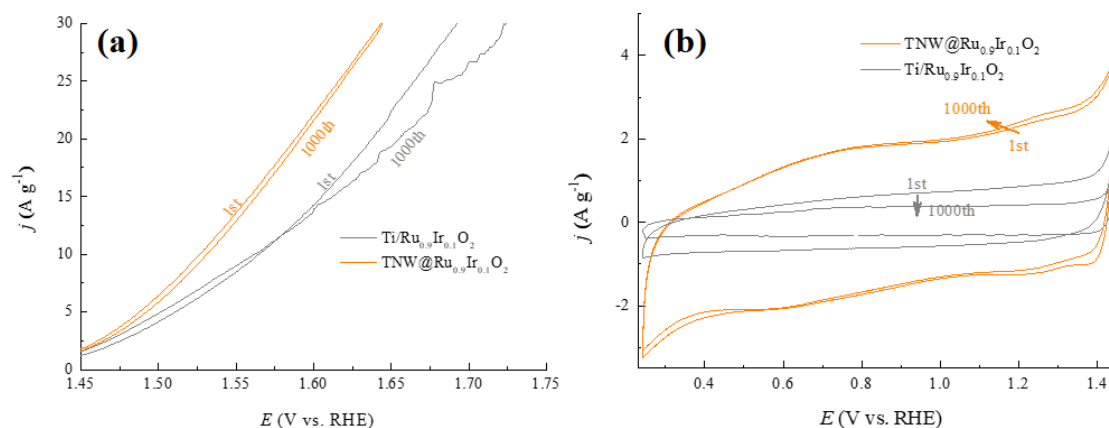


**Figure 6.** (a) LSV and (b) CV curves of Ti/Ru<sub>0.9</sub>Ir<sub>0.1</sub>O<sub>2</sub> and TNW@Ru<sub>0.9</sub>Ir<sub>0.1</sub>O<sub>2</sub> electrodes. The scanning rates of 1st and 1000th cycles is 20 mV s<sup>-1</sup>, and the intermediate cycles are 100 mV s<sup>-1</sup>.

So, the introduction of TiO<sub>2</sub> nanostructures benefits to enhance the long-term durability of electrode materials. There are two main factors that might contribute to this phenomenon. On one hand, TiO<sub>2</sub> nanowires grown by in-situ hydrothermal method on the Ti matrix bonds robustly to the active materials RuO<sub>2</sub>/IrO<sub>2</sub> compared to the bare Ti matrix. On the other hand, TiO<sub>2</sub> nanostructured template, which is beneficial to the formation of RuO<sub>2</sub>/IrO<sub>2</sub> mixed nanocrystals, effectively avoids the abundant cracks forming on the coating surface.

#### 4. CONCLUSIONS

In summary, RuO<sub>2</sub>/IrO<sub>2</sub> mixed nanocrystal loading on the various TiO<sub>2</sub> nanostructures have been successfully synthesized by a combination of hydrothermal method and thermal pyrolysis. With the introduction of TiO<sub>2</sub> nanowires, the OER potential of electrode at 30 A g<sup>-1</sup> significantly decreases, the electrochemically active surface area is boosted, suggesting that the higher catalytic activity is verified. Furthermore, the inserting of TiO<sub>2</sub> nanostructures between Ti matrix and catalytic coating can enhance the cyclic stability in the acid solution.

#### References

1. G.H. Rau, H.D. Willauer, Z.J. Ren. *Nat. Clim. Change*, 8 (2018) 621.
2. D. Voiry, H.S. Shin, K.P. Loh, M. Chhowalla. *Nat. Rev. Chem.*, 2(2018) 0105.
3. B. You, Y. Sun. *Accounts Chem. Res.*, 51(2018) 1571.
4. I. Roger, M.A. Shipman, M.D. Symes. *Nat. Rev. Chem.*, 1 (2017) 0003.

5. B.M. Hunter, H.B. Gray, A.M. Muller. *Chem. Rev.*, 116 (2016) 14120-14136.
6. N.T. Suen, S.F. Hung, Q. Quan, N. Zhang, Y.J. Xu, H.M. Chen. *Chem. Soc. Rev.*, 46 (2017) 337.
7. K. Mamtani, D. Jain, D. Dogu, V. Gustin, S. Gunduz, A.C. Co, U.S. Ozkan. *Appl. Catal. B- Environ.*, 220 (2018) 88.
8. E. Oakton, D. Lebedev, M. Povia, D.F. Abbott, E. Fabbri, A. Fedorov, M. Nachtegaal, C. Copéret, T.J. Schmidt. *ACS Catal.*, 7 (2017) 2346.
9. C. Zhang, J. Sha, H. Fei, M. Liu, S. Yazdi, J. Zhang, Q. Zhong, X. Zou, N. Zhao, H. Yu. *ACS Nano*, 11 (2017) 6930.
10. T. Reier, M. Oezaslan, P. Strasser. *ACS Catal.*, 2 (2012)1765.
11. J. Zhang, B. Yuan, S. Cui, N. Zhang, J. Wei, X. Wang, D. Zhang, R. Zhang, Q. Huo. *Dalton T.*, 46 (2017) 3295.
12. F. Dionigi, P. Strasser. *Adv. Energy Mater.*, 6 (2016) 1600621.
13. C. Hu, L. Dai. *Adv. Mater.*, 29 (2017) 1604942.
14. K. Liu, C. Zhang, Y. Sun, G. Zhang, X. Shen, F. Zou, H. Zhang, Z. Wu, E.C. Wegener, C.J. Taubert, J.T. Miller, Z. Peng, Y. Zhu. *ACS Nano*, 12 (2018) 158.
15. Y. Zhao, B. Jin, A. Vasileff, Y. Jiao, S.Z. Qiao. *J. Mater. Chem. A*, 7 (2019) 8117.
16. J. Dai, Y. Zhu, Y. Zhong, J. Miao, B. Lin, W. Zhou, Z. Shao. *Adv. Mater. Inter.*, 6 (2019) 1801317.
17. J. Wang, Y. Gao, D. Chen, J. Liu, Z. Zhang, Z. Shao, F. Ciucci. *ACS Catal.*, 8 (2017) 364.
18. T. Maiyalagan, K.A. Jarvis, S. Therese, P.J. Ferreira, A. Manthiram. *Nat. Comm.*, 5 (2014) 3949.
19. Y. Wang, C. Xie, Z. Zhang, D. Liu, R. Chen, S. Wang. *Adv. Funct. Mater.*, 28 (2018)1703363.
20. T. Reier, H.N. Nong, D. Teschner, R. Schlögl, P. Strasser. *Adv. Energy Mater.*, 7 (2017) 1601275.
21. C. Spoen, J.T.H. Kwan, A. Bonakdarpour, D.P. Wilkinson, P. Strasser. *Angew. Chem. Int. Edit.*, 56 (2017) 5994.
22. N. Danilovic, R. Subbaraman, K.C. Chang, S.H. Chang, Y.J. Kang, J. Snyder, A.P. Paulikas, D. Strmcnik, Y.T. Kim, D. Myers. *J. Phys. Chem. Lett.*, 5 (2014) 2474.
23. L.C. Seitz, C.F. Dickens, Nishio K., Y. Hikita, J. Montoya, A. Doyle, C. Kirk, A. Vojvodic, H.Y. Hwang, J.K. Norskov. *Science*, 353 (2016) 1011.
24. J. Shan, C. Guo, Y. Zhu, S. Chen, L. Song, M. Jaroniec, Y. Zheng, S.Z. Qiao. *Chem*, 5 (2019) 445.
25. J. Lim, D. Park, S.S. Jeon, C.W. Roh, J. Choi, D. Yoon, M. Park, H. Jung, H. Lee. *Adv. Funct. Mater.*, 28 (2018) 1704796.
26. J. Su, R. Ge, K. Jiang, Y. Dong, F. Hao, Z. Tian, G. Chen, L. Chen. *Adv. Mater.*, 30 (2018) 1801351.
27. S. Cherevko, S. Geiger, O. Kasian, N. Kulyk, J.P. Grote, A. Savan, B.R. Shrestha, S. Merzlikin, B. Breitbach, A. Ludwig. *Catal. Today*, 262 (2016) 170.
28. C.J. Chang, Y.C. Chu, H.Y. Yan, Y.F. Liao, H.M. Chen. *Dalton T.*, 48 (2019) 7122.
29. S.J. Kim, Y.K. Cho, J. Seok, N.S. Lee, B. Son, J.W. Lee, J.M. Baik, C. Lee, Y. Lee, M.H. Kim. *ACS Appl. Mater. & Interf.*, 7 (2015) 15321.
30. G. Li, S. Li, J. Ge, C. Liu, W. Xing. *J. Mater. Chem. A*, 5 (2017) 17221.
31. J. Shan, C. Guo, Y. Zhu, S. Chen, L. Song, M. Jaroniec, Y. Zheng, S.-Z. Qiao. *Chem*, 5 (2019) 445.
32. R.F. Savinell, R.L. Zeller III, J.A. Adams. *J. Electrochem. Soc.*, 137 (1991) 489.
33. S. Trasatti, O.A. Petrii. *Pure Appl. Chem.*, 63 (1991) 711.
34. C.C.L. McCrory, S. Jung, J.C. Peters, T.F. Jaramillo. *J. Am. Chem. Soc.*, 135 (2013) 16977.